Supporting Information for the manuscript:

Vanadyl spin qubits 2D arrays and their integration on superconducting resonators

Ainhoa Urtizberea, Eva Natividad, Pablo J. Alonso, Laura Pérez-Martínez, Miguel A. Andrés, Ignacio Gascón, Ignacio Gimeno, Fernando Luis and Olivier Roubeau

Table of contents:

A) Infra-red spectroscopy

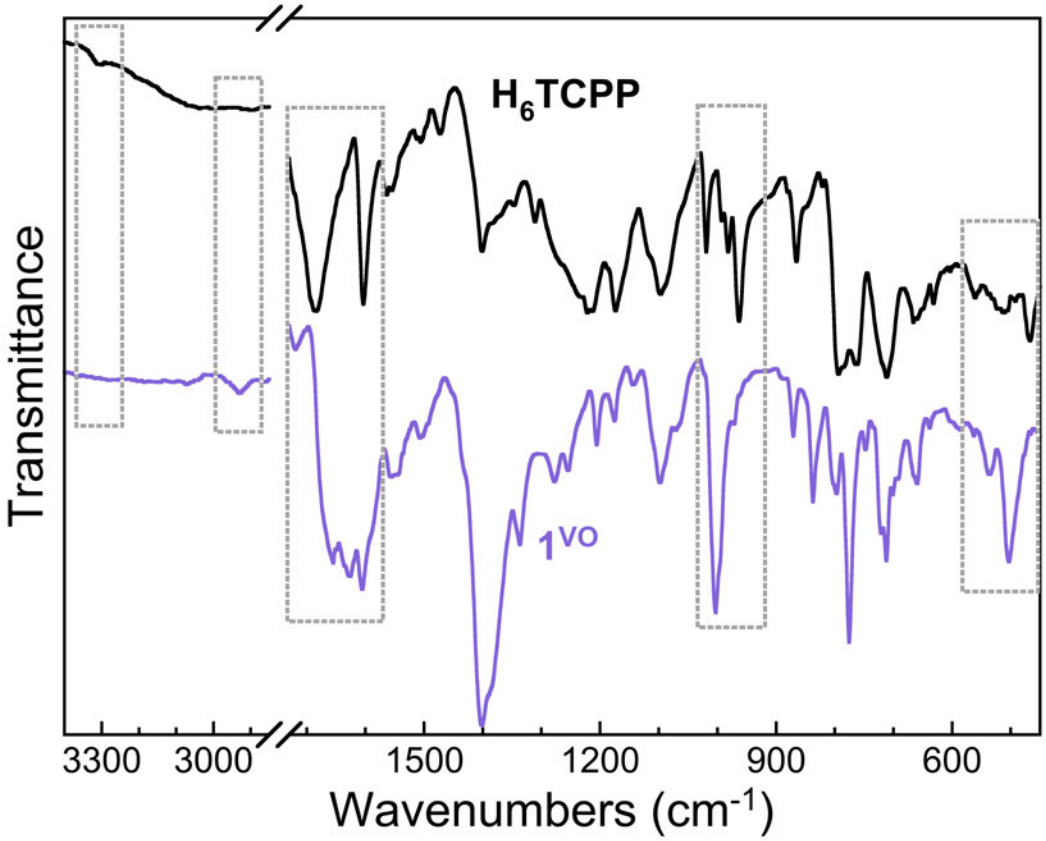

Figure S1. Infra-red spectra of H_6TCPP and **1**^{VO}. The grey dashed rectangles highlight areas with modifications associated with the coordination of H_6TCPP.

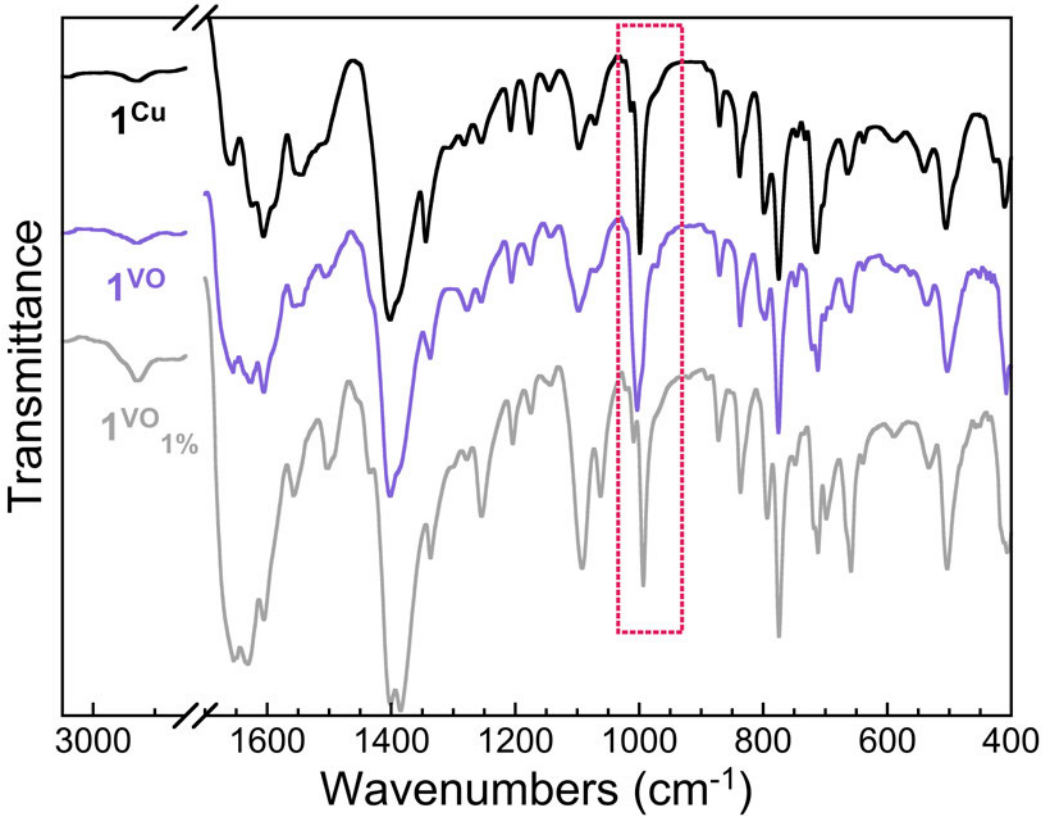

Figure S2. Infra-red spectra of $\mathbf{1}^{VO}$ and the magnetically-diluted $\mathbf{1}^{VO}_{1\%}$, compared with that of the Cu(II) analogue $\mathbf{1}^{Cu}$. The red dashed rectangle highlights the characteristic band indicative of metallated porphyrin rings.

B) Powder X-ray diffraction

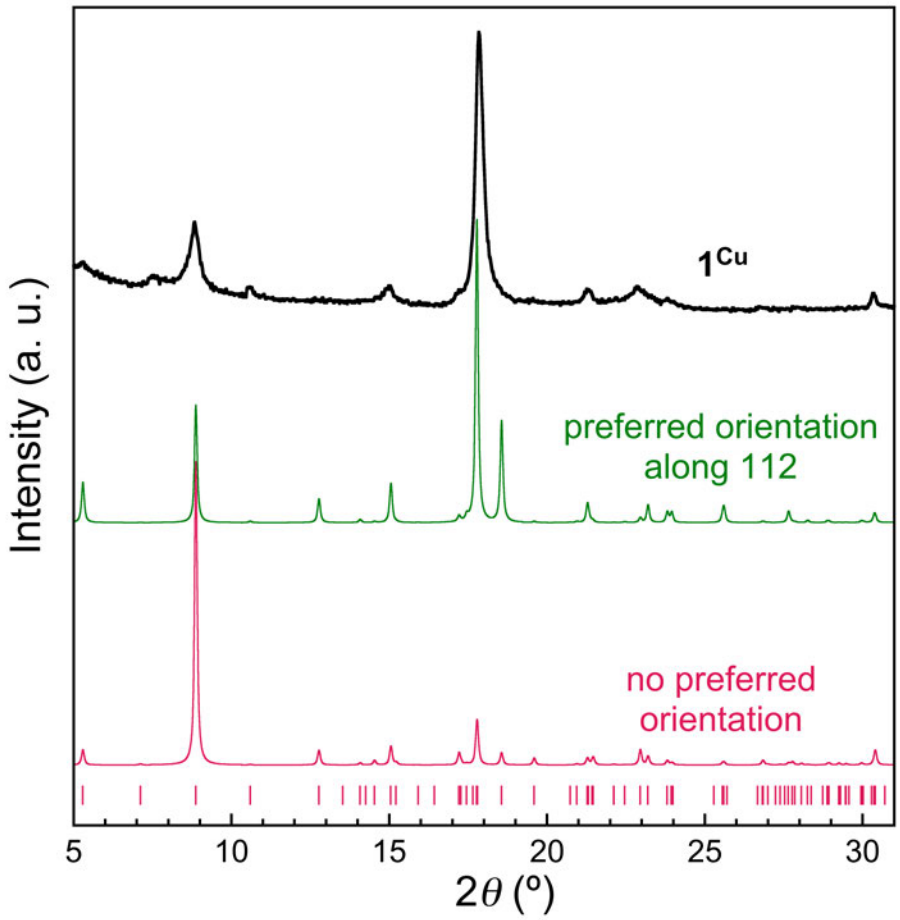

Figure S3A. Powder X-ray diffraction patterns of $\mathbf{1}^{\mathbf{Cu}}$ (top, black line) compared with the calculated patterns using the reported single-crystal structure (CCDC 1555581, bottom, red line).[1] While the agreement of the experimental patterns with the positions of the hkl reflections from the reported structure (red ticks at the bottom) is reasonable, there are clear discrepancies in term of relative intensities of the main diffraction peaks. These can mostly be accounted for by taking into account the effect of preferential orientation crystallites along the 112 direction (middle, green line). Remaining slight differences likely originate in the presence of several preferential orientations, and from the possible differences in lattice solvent content between the single-crystals freshly out of their mother solution and the dry powder. Indeed, the lattice solvent dmf was found to be disordered / diffuse in the reported structure of $\mathbf{1}^{\mathbf{Cu}}$.[1]

[1] A. Urtizberea, E. Natividad, P. J. Alonso, M. A. Andrés, I. Gascón, M. Goldmann, O. Roubeau, *Adv. Funct. Mater.*, 2018, **28**, 1801695.

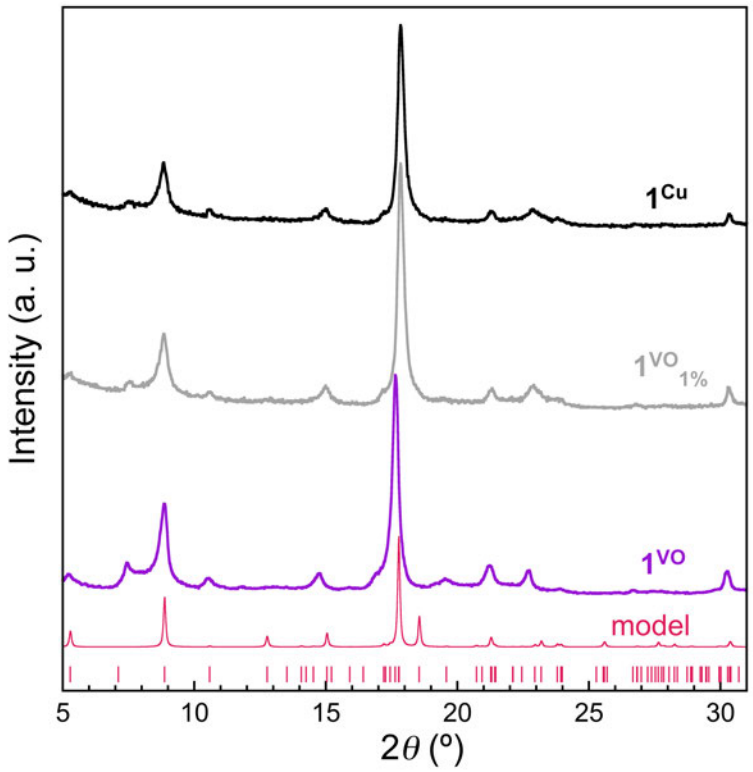

Figure S3B. Powder X-ray diffraction patterns of $\mathbf{1}^{VO}$ (middle, violet line) and $\mathbf{1}^{VO}{}_{1\%}$ (middle, grey line) compared with those for $\mathbf{1}^{Cu}$ (top, black line) and the calculated patterns for a structural model (bottom, red line), that uses the single-crystal structure of $\mathbf{1}^{Cu}$, except for the Cu(II) site at 0, 1, 0 coordinates that is replaced by a vanadyl moiety slightly off the porphyrin plane with coordinates -0.0340, 1, 0.0296 for the V site and -0.1390, 1, 0.1290 for the O site. The same preferential orientation along the 112 direction has been included in the simulated patterns. Positions of the model hkl reflections are shown as red ticks at the bottom.

C) Static magnetic susceptibility

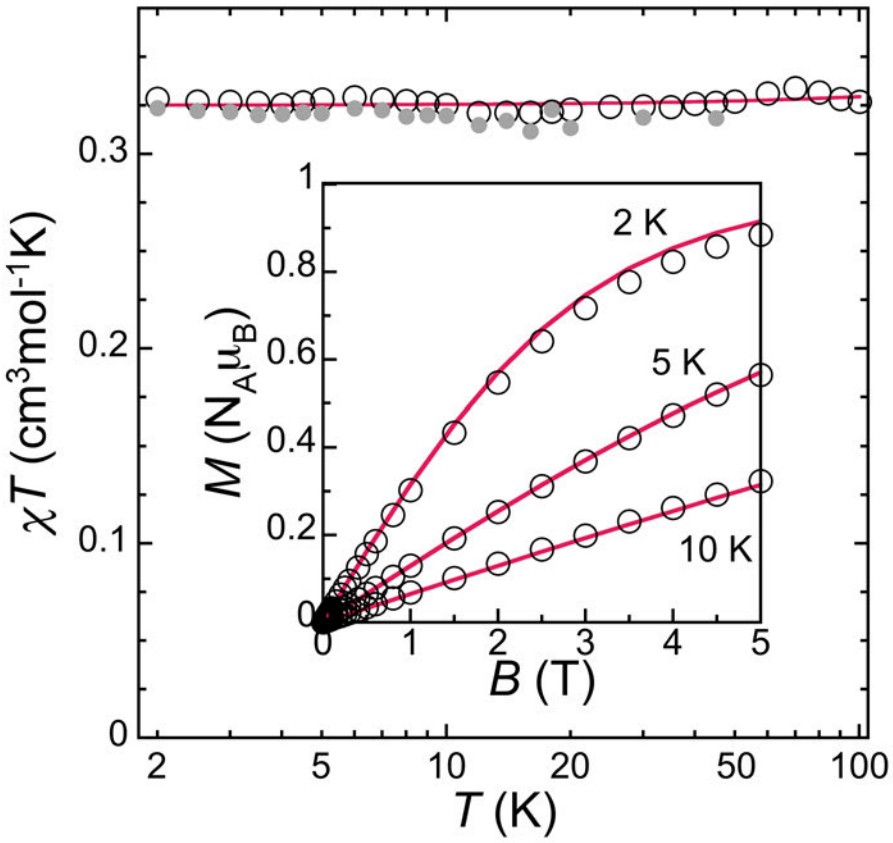

Figure S4. Temperature dependence of χT for $\mathbf{1}^{vo}$ as derived from *dc* measurements at 0.01 T (empty symbols) and zero-field *ac* measurements at 10 Hz (full gray symbols). The solid red line represents the Curie law for C = 0.325 cm^3mol^{-1}. Inset: Magnetization isotherms at the indicated temperatures for $\mathbf{1}^{vo}$ with corresponding Brillouin functions for S = 1/2 and g = 1.97 depicted as red lines.

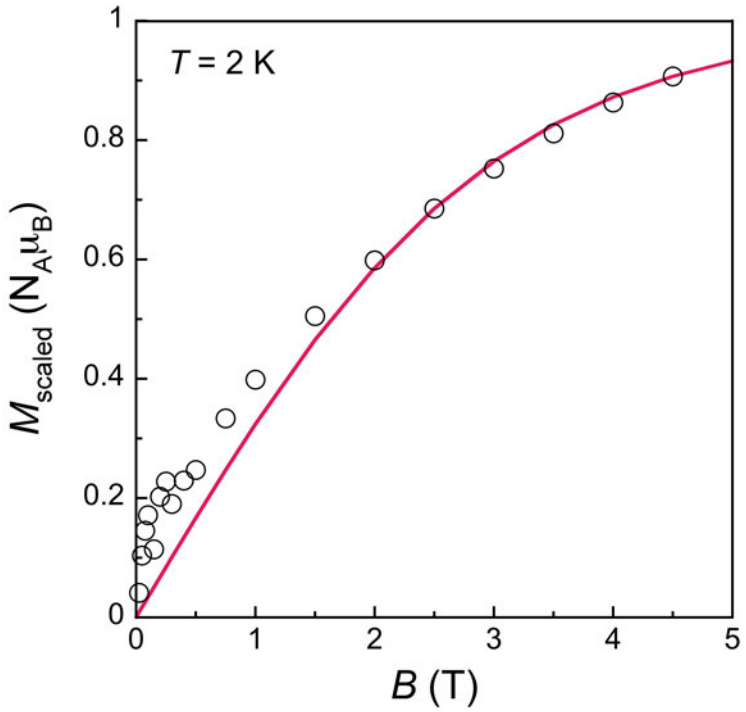

Figure S5. Magnetization *vs.* field isotherm of a 40-layers [{VO(TCPP)}Zn_2] nanosheets deposit on Mylar at 2 K, scaled to molar units by considering a mass of 5.5 x 10^{-5} g of $\mathbf{1}^{\mathbf{VO}}$. The solid red lines correspond to the Brillouin function for S = 1/2 and g = 2.0. Considering the total area of the measured Mylar sheet of *ca*. 340 mm^2 the derived scale factor translate into ca. 8.92 x 10^{15} spins cm^{-2}. Considering the surface density of the 2D planes in $\mathbf{1}^{\mathbf{VO}}$, one $V^{IV}O$ spin per *ca.* 2.9 nm^2, this corresponds to 75 molecular planes, i.e. an average of 1.88 per transfer cycle.

D) ac magnetic susceptibility

The spin-lattice relaxation time T_1^{ac} was extracted from the frequency dependence of the real and imaginary components of the *ac* susceptibility χ' and χ'' using the following expressions corresponding to the generalized Debye model:

$$\chi'(\omega) = \chi_S + (\chi_T - \chi_S)\frac{1 + (\omega\tau)^{\beta}\cos\left(\frac{\pi\beta}{2}\right)}{1 + 2(\omega\tau)^{\beta}\cos\left(\frac{\pi\beta}{2}\right) + (\omega\tau)^{2\beta}}$$

$$\chi''(\omega) = (\chi_T - \chi_S)\frac{(\omega\tau)^{\beta}\sin\left(\frac{\pi\beta}{2}\right)}{1 + 2(\omega\tau)^{\beta}\cos\left(\frac{\pi\beta}{2}\right) + (\omega\tau)^{2\beta}}$$

in which ω is the angular frequency, χ_T the isothermal susceptibility, χ_S the adiabatic susceptibility and β describes the distribution of relaxation times. β was found to be in the range 0.5-0.85, indicating the presence of a significant distribution of relaxation times.

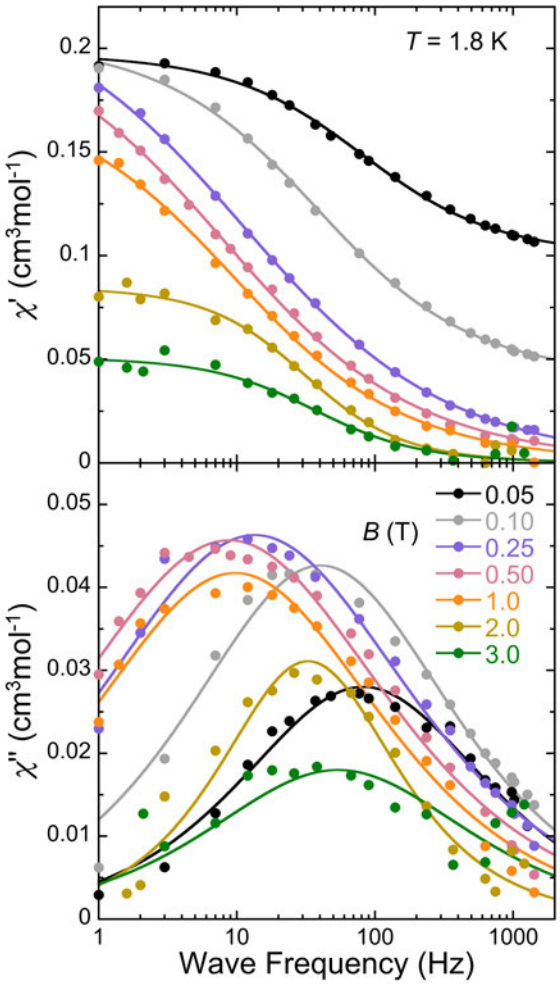

Figure S6. Frequency dependence of the in-phase (top) and out-of-phase (bottom) *ac* magnetic susceptibility of **1**^{VO} at 1.8 K and variable applied *dc* fields. Lines are fits of the experimental data to the Cole-Cole expressions for the real and imaginary susceptibility.

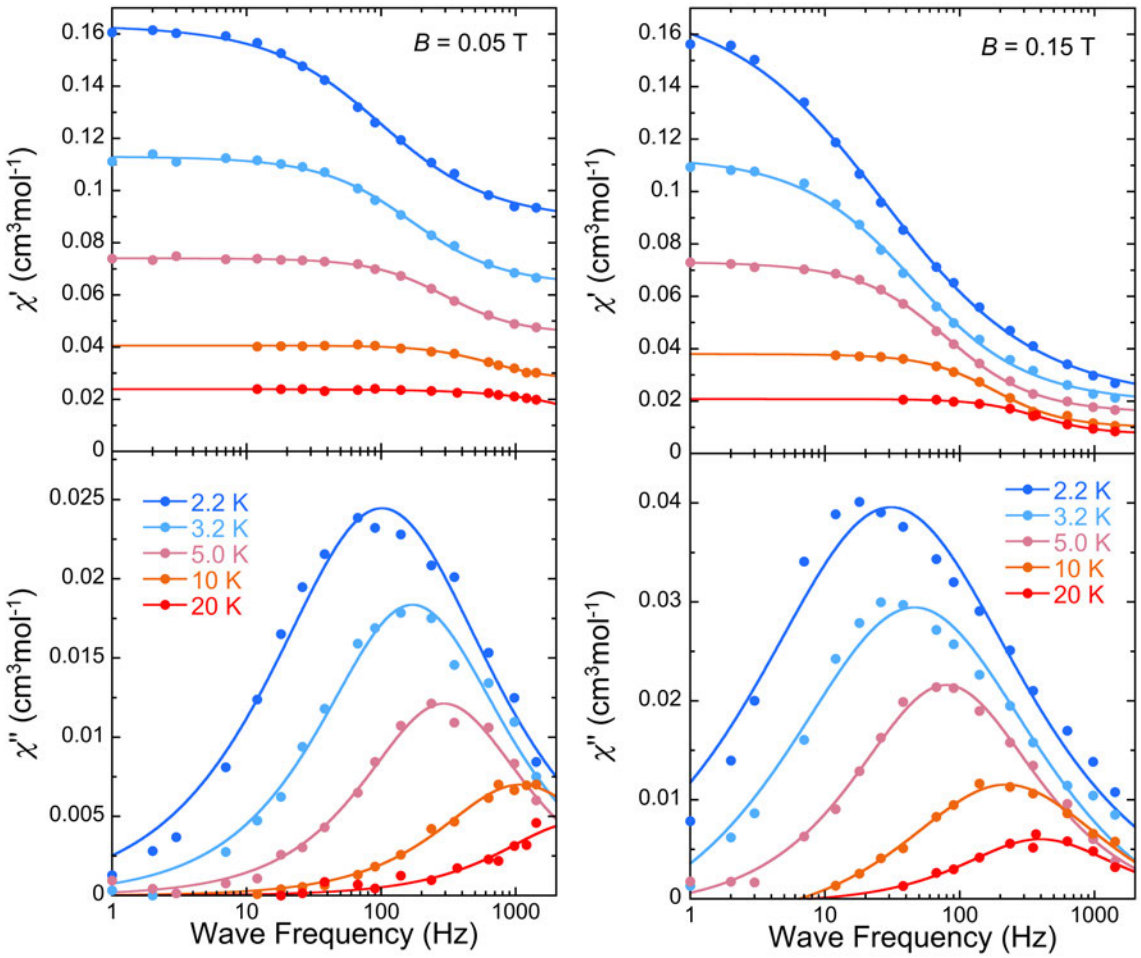

Figure S7. Frequency dependence of the in-phase (top) and out-of-phase (bottom) *ac* magnetic susceptibility of **1**^{VO} at 0.05 and 0.15 T applied *dc* field and variable temperature. Lines are fits of the experimental data to the Cole-Cole expressions for the real and imaginary susceptibility.

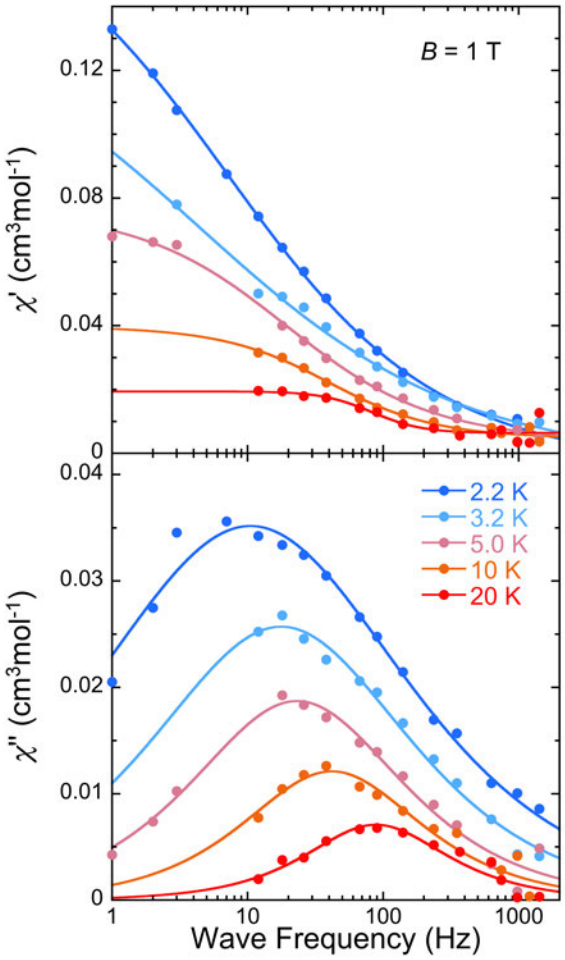

Figure S8. Frequency dependence of the in-phase (top) and out-of-phase (bottom) *ac* magnetic susceptibility of **1**^{VO} at 1 T applied *dc* field and variable temperature. Lines are fits of the experimental data to the Cole-Cole expressions for the real and imaginary susceptibility.

E) Electron Paramagnetic Resonance spectroscopy

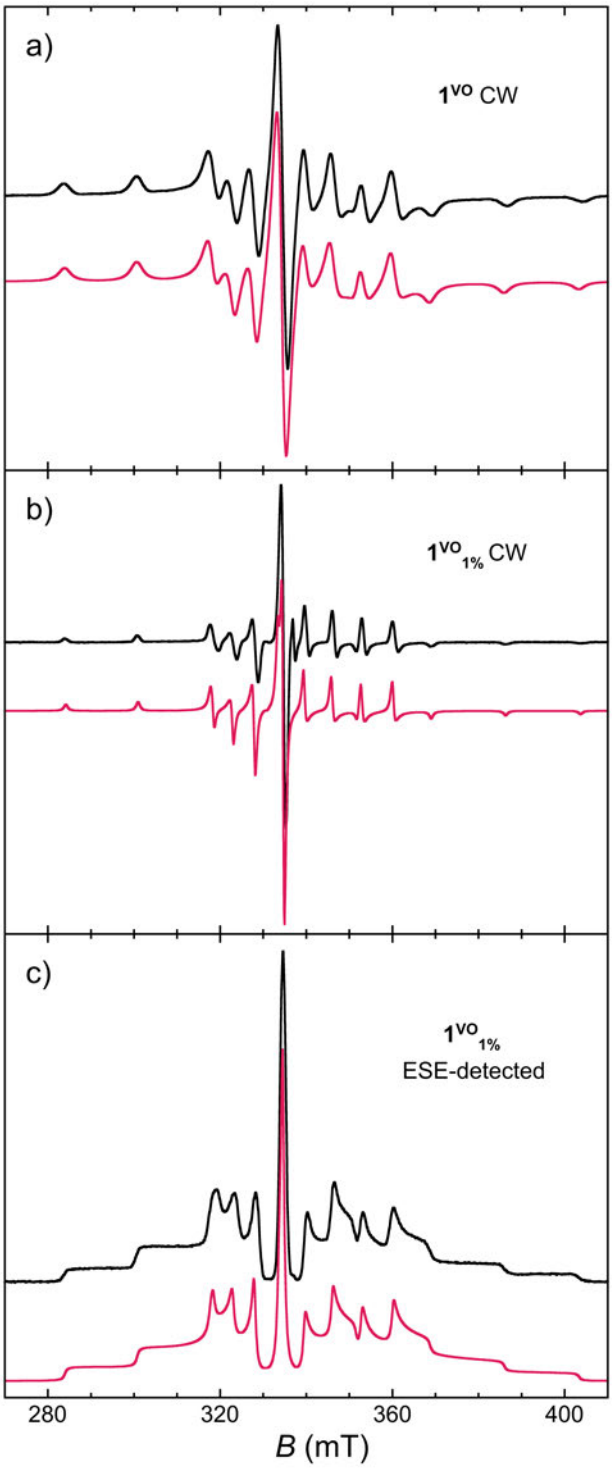

Figure S9. Comparison between the observed cw-EPR spectrum of **1**^{VO} at RT (a, black trace), **1**$^{VO}_{1\%}$ at 6 K (b, black trace) and 2p-ei-EPR (τ = 200 ns) spectrum of **1**$^{VO}_{1\%}$ at 80 K (c, black trace) with the ones simulated (red traces) using an axial spin Hamiltonian with $g_{\parallel}$ = 1.969, $g_{\perp}$ = 1.99, $A_{\parallel}$ = 470 MHz and $A_{\perp}$ = 165 MHz and a lorenztian linewidth with ΔH = 2.0 mT (a), ΔH = 0.6 mT (b) and ΔH = 0.5 mT (c).

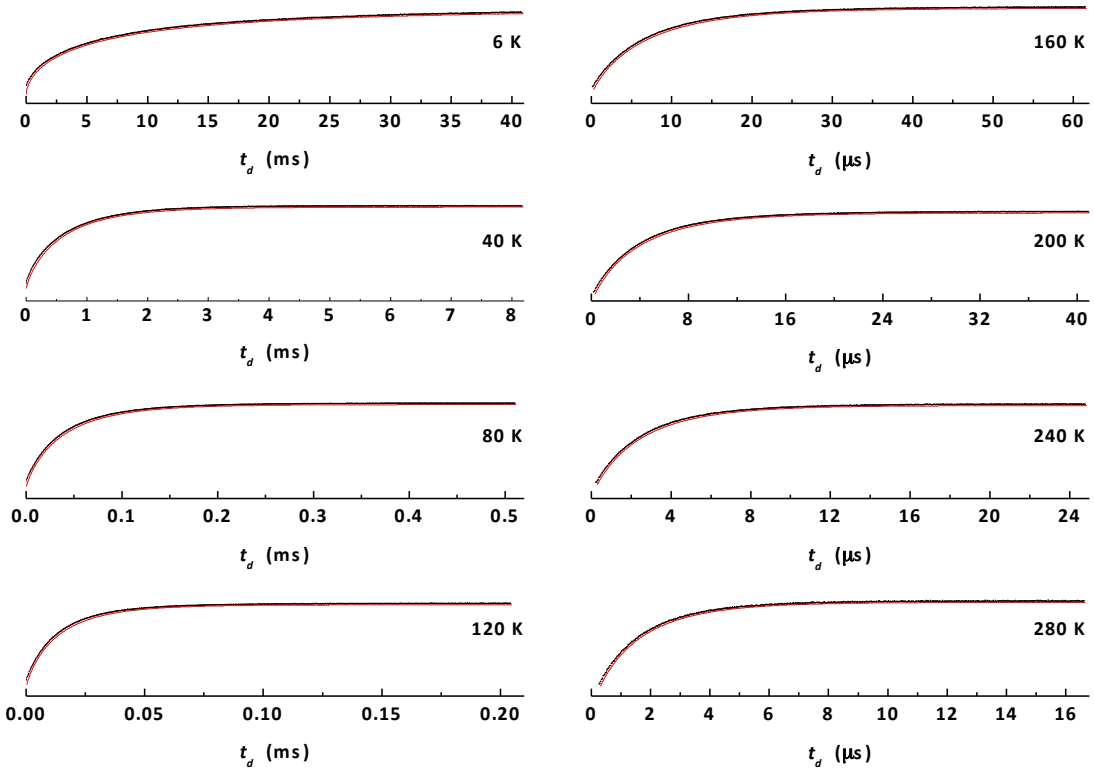

Figure S10. ESE detected Inversion Recovery as a function of delay time, t_d, for $\mathbf{1}^{VO}_{1\%}$ at 343.3 mT and selected temperatures (circles). Red lines correspond to a stretched exponential t_d dependence modeled by:

$$y(t_d) = y_\infty - y_0 e^{-\left(t_d/\beta T_1'\right)^\beta}$$

that best fit to the data. The values of the relevant best-fit parameters are gathered in Table S1.

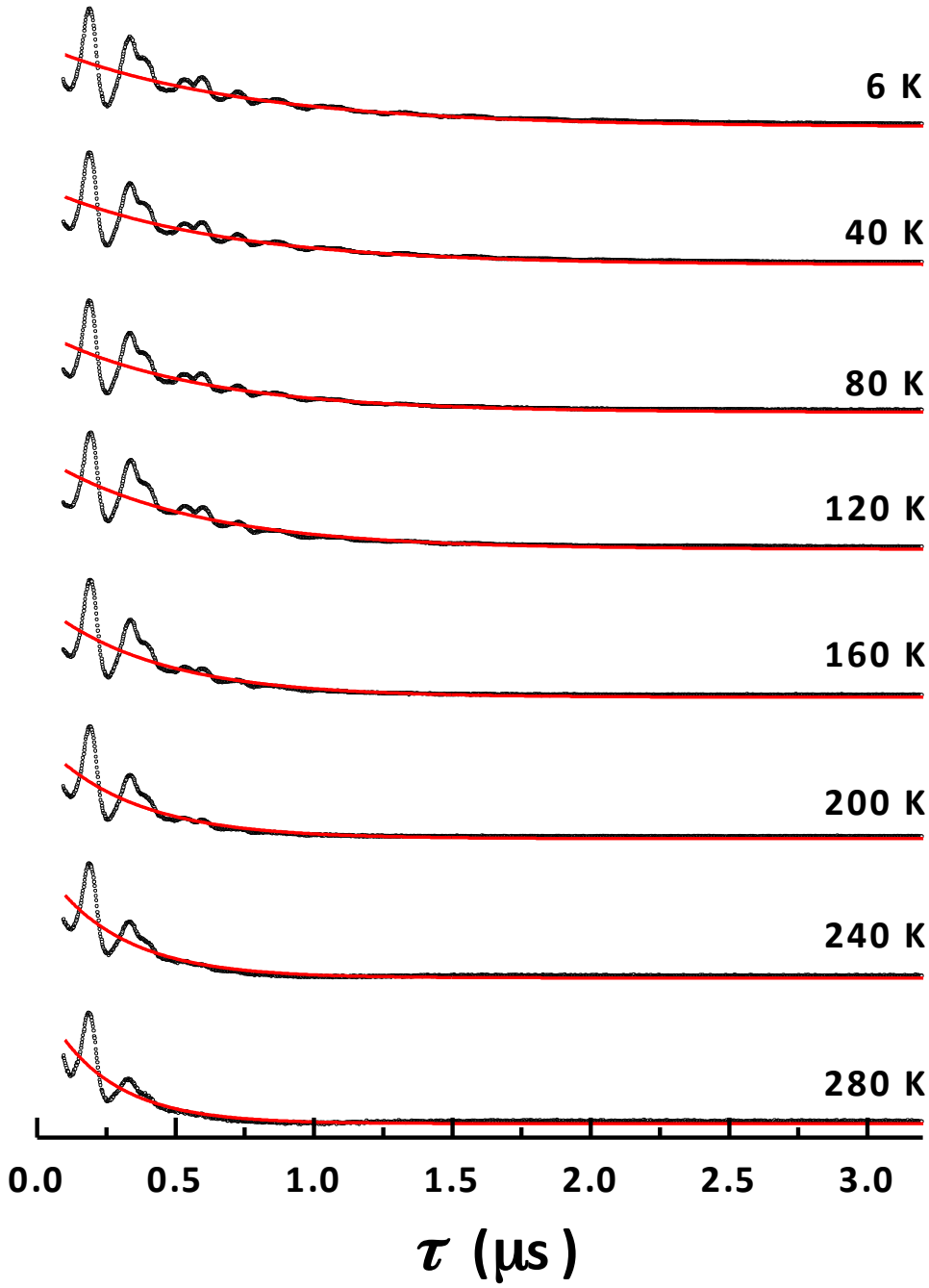

Figure S11. 2p ESE intensity as a function of inter-pulse interval, τ, for $\mathbf{1}^{\mathbf{VO}}_{\mathbf{1\%}}$ at 343.3 mT and selected temperatures (circles). Red lines correspond to the evolution predicted with an exponential decay expressed as:

$$y(\tau) = y_0 + A_{2p} e^{-2\tau/T_M}$$

with the values of the parameters that give the best fit gathered in Table S1.

Table S1. Parameters that provide the best fits to ESE detected Inversion Recovery signals and the 2p-ESE decay for $\mathbf{1}^{VO}_{1\%}$ measured at 343.3 mT and variable temperature.

T (K)	T_1' (μs)	β	T_M (μs)
6	10,690 ± 40	0.59	1.43 ± 0.06
10	6,441 ± 30	0.63	1.37 ± 0.06
20	2,477 ± 10	0.74	1.34 ± 0.06
30	1,432 ± 8	0.75	1.32 ± 0.06
40	720 ± 4	0.82	1.29 ± 0.06
50	394 ± 4	0.85	1.24 ± 0.06
60	217 ± 4	0.88	1.16 ± 0.06
70	103 ± 3	0.93	1.09 ± 0.06
80	60 ± 2	0.87	1.11 ± 0.06
90			1.11 ± 0.06
100	29.0 ± 0.1	0.83	1.10 ± 0.06
110			1.15 ± 0.06
120	16.3 ± 0.1	0.83	1.08 ± 0.06
130			1.08 ± 0.06
140	11.2 ±0.2	0.83	0.99 ± 0.06
150			0.91 ± 0.06
160	8.0 ±0.3	0.84	0.83 ± 0.05
170			0.79 ± 0.04
180	5.8 ± 0.4	0.86	0.73 ± 0.04
190			0.69 ± 0.04
200	4.5 ± 0.4	0.86	0.66 ± 0.04
210			0.61 ± 0.04
220	3.4 ±0.6	0.86	0.59 ± 0.04
230			0.57 ± 0.04
240	2.7 ± 0.8	0.87	0.55 ± 0.04
250			0.54 ± 0.04
260	2.0 ± 0.9	0.88	0.52 ± 0.04
270			0.50 ± 0.04
280	1.7 ± 1.2	0.87	0.46 ± 0.04
300	1.4 ± 1.4	0.87	

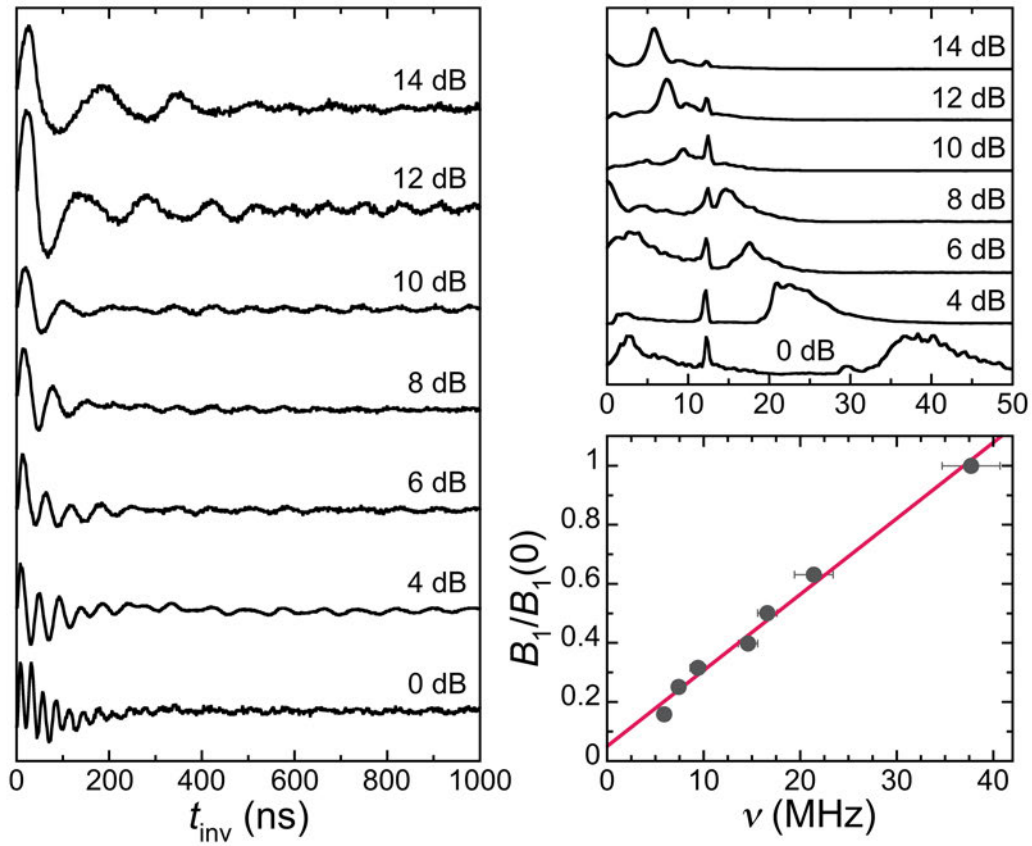

Figure S12. Left: Rabi oscillations recorded at 80 K for $\mathbf{1}^{VO}_{1\%}$ in the crystal-like line at 291.5 mT and for increasing microwave attenuations. Right: Fourier transform (power spectrum) of these nutation signals (top) and frequency dependence of the frequency of the maximum with the relative microwave magnetic field, $B_1/B_1(0)$, (bottom).

F) Transmission Electron Microscopy

TEM images show the grid carbon layer with very weak superimposed fringes, which presumably correspond to the MOF lattice spacings. In order to quantify these spacings, FFTs of small image areas (35.72 x 35.72 nm^2, of the order of one nanodomain) were analysed to enhance the apparition of reciprocal points (Figure S13). Since reciprocal points were still weak, up to 21 areas were analysed, giving rise to 81 distance values. In our previous work,[1] it was shown that, even though the carbon layer is amorphous, its typical pattern can originate some weak points in the reciprocal space, especially at 20-21 nm, followed by 34-35 nm and 45-46 nm. Consequently, distances over 20 Å were not considered.

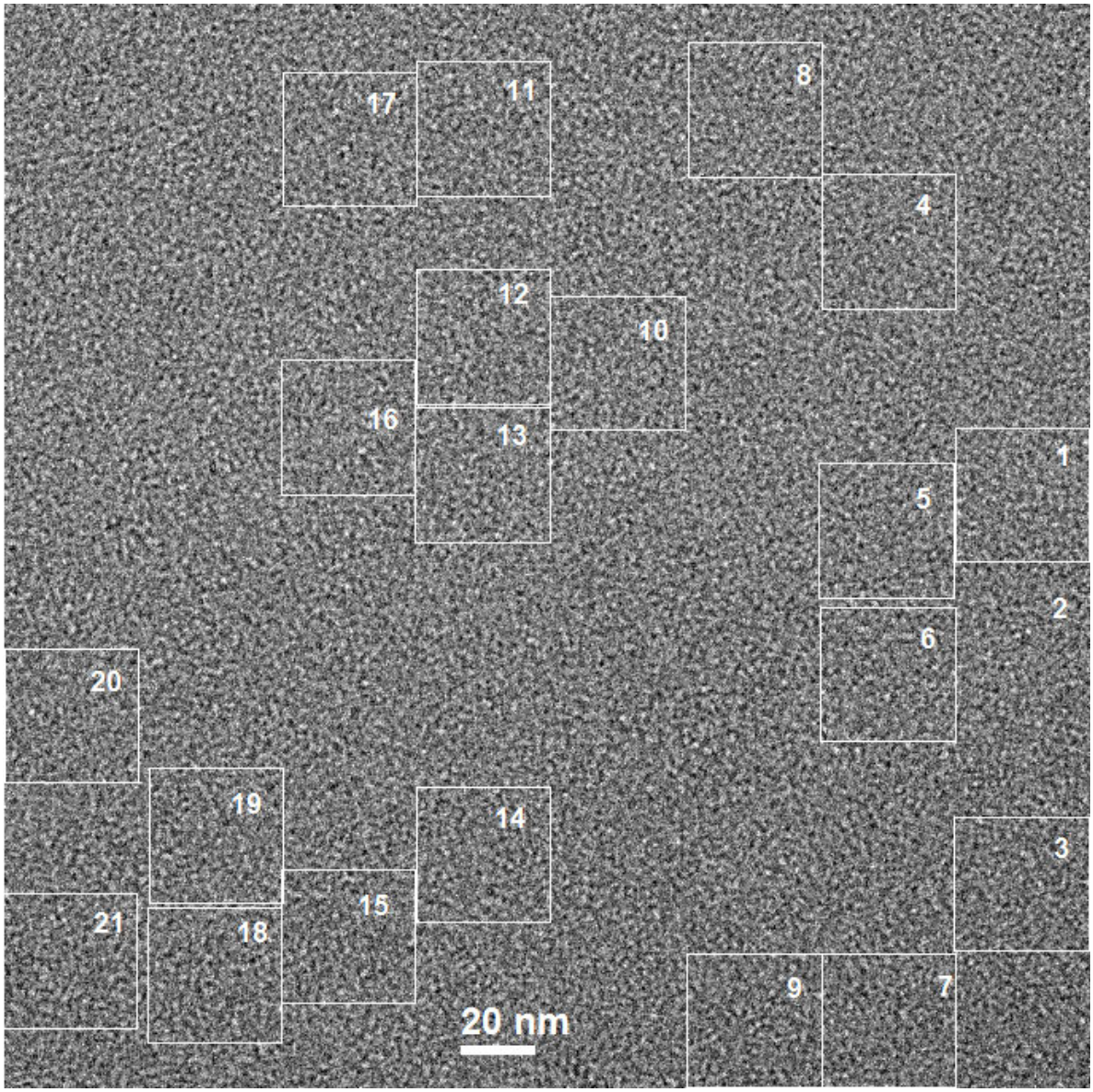

Figure S13. Characteristic TEM image of 1-layer MOF film, with the 21 areas analysed by FFT (see Figures S14 and S15).

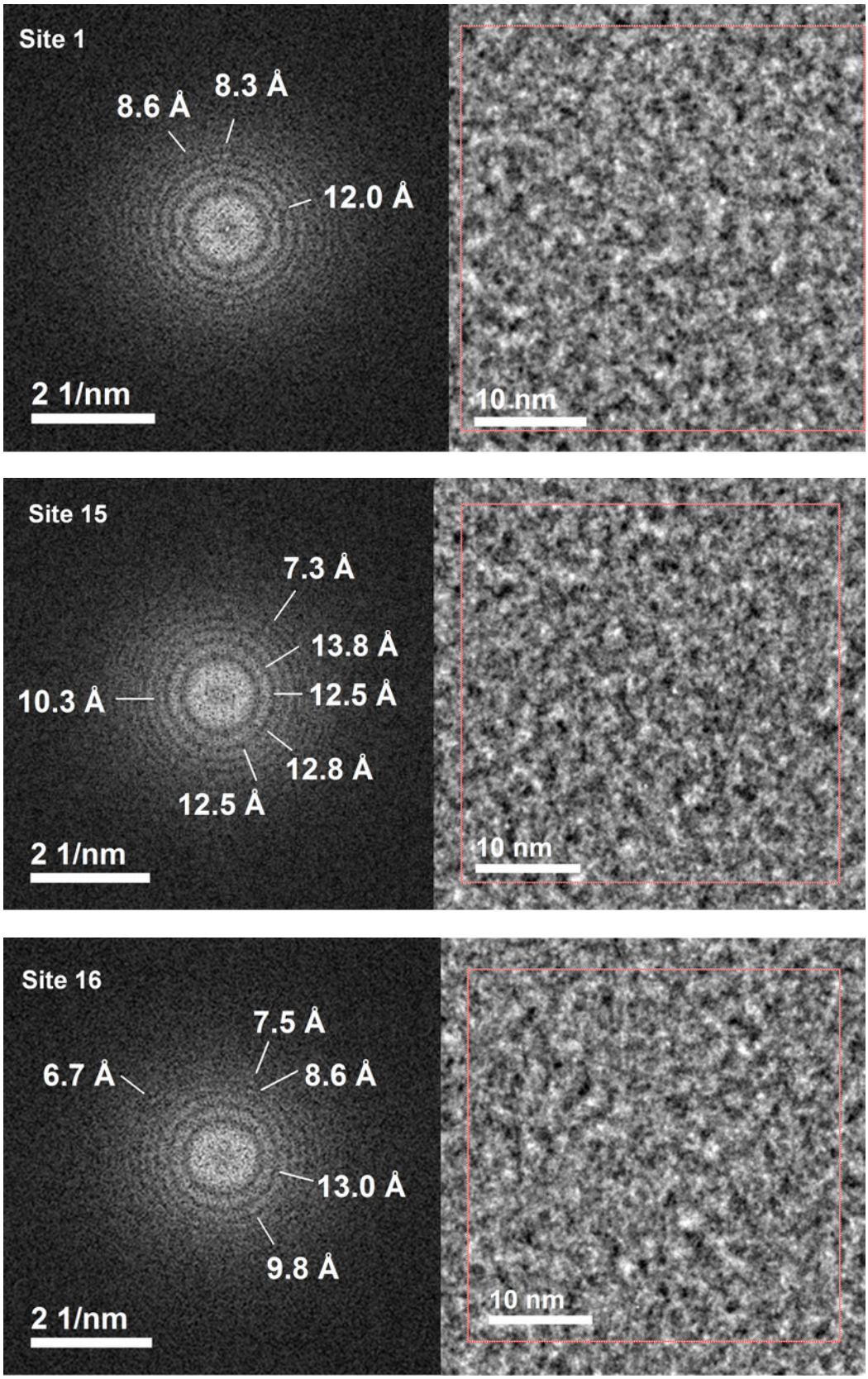

Figure S14. Examples of FFTs of small areas in the TEM image in Figure S13.

A common histogram representation (constant bin interval) of the obtained data did not derive any clear conclusion about the crystallinity of the film. Then data was represented according to their order number (Figure S15, from the lowest distance to the highest) with the aim of inferring whether data were continuous or presented steps (discrete values with dispersion). Since data fulfilled the later, average values and standard deviation of values in each step (enclosed in rectangles, ± 0.5 Å) were calculated. With these data, a new histogram was constructed (inset in Figure S15), including 85% of the data.

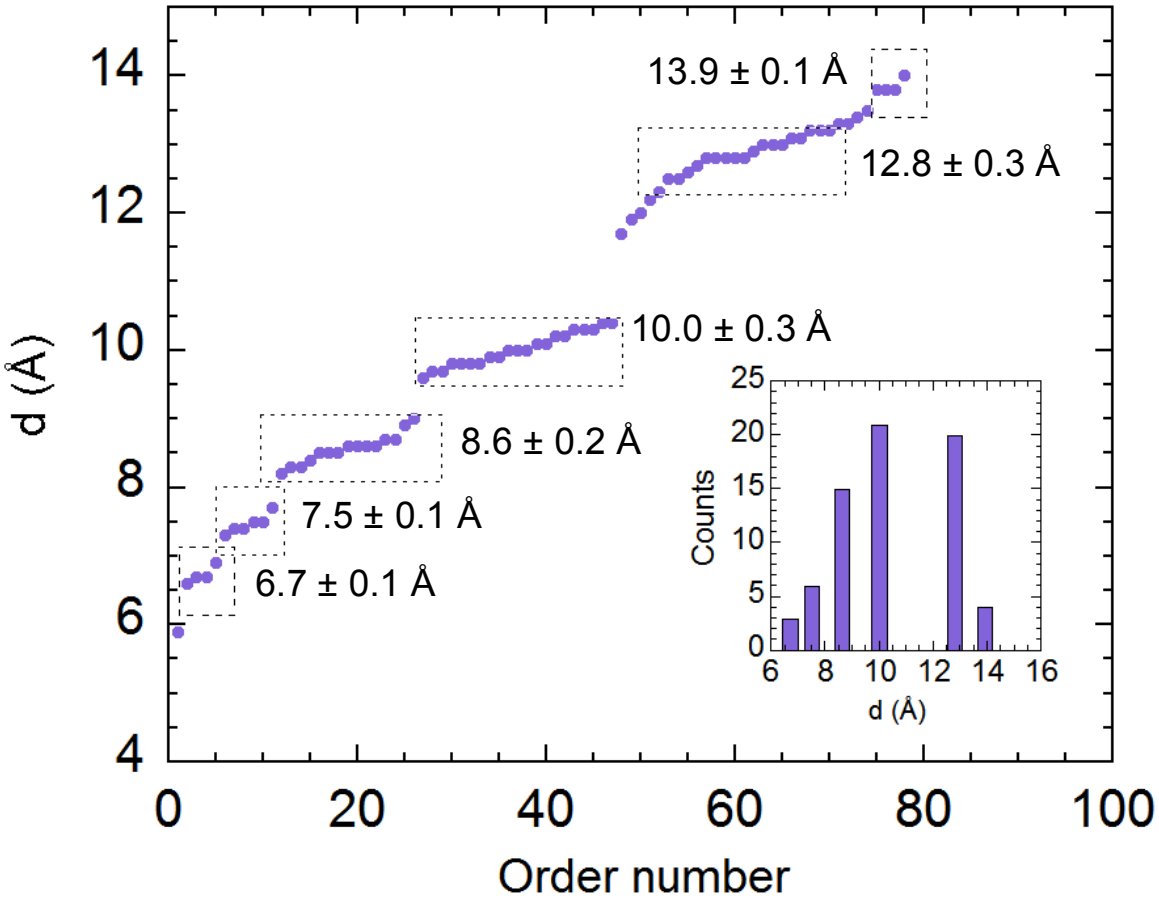

Figure S15. Distances obtained from FFTs ordered from the lowest to the highest. Inset: histogram obtained from the average value and standard deviation of the steps (rectangles).

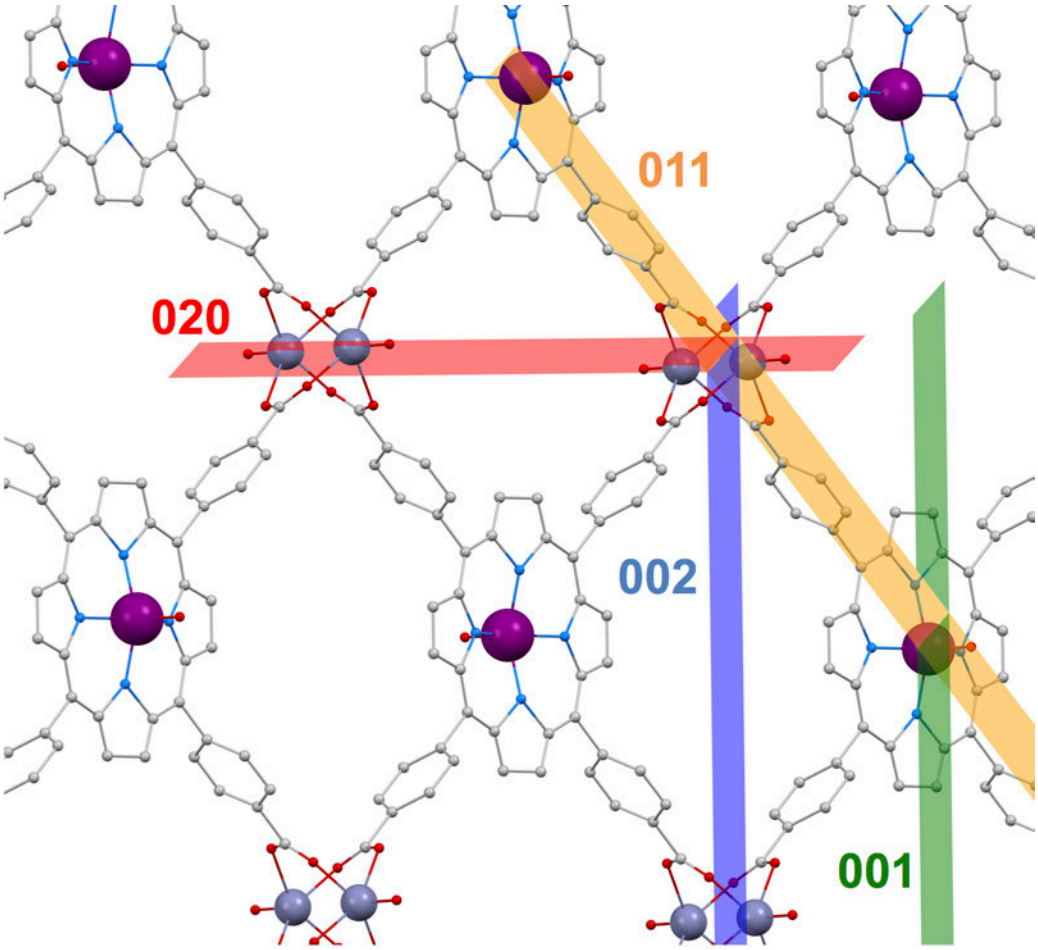

Figure S16. View of a portion of 2D plane in the structure of **1**^{VO} highlighting the *hkl* planes coinciding with characteristic reciprocal distances found in FFT analysis of the TEM image. Colour code: V, violet spheres; Zn, blue-grey spheres; N, lighter blue small spheres; C, grey small spheres. Hydrogens are omitted for clarity.

G) X-ray Photo-electron Spectroscopy

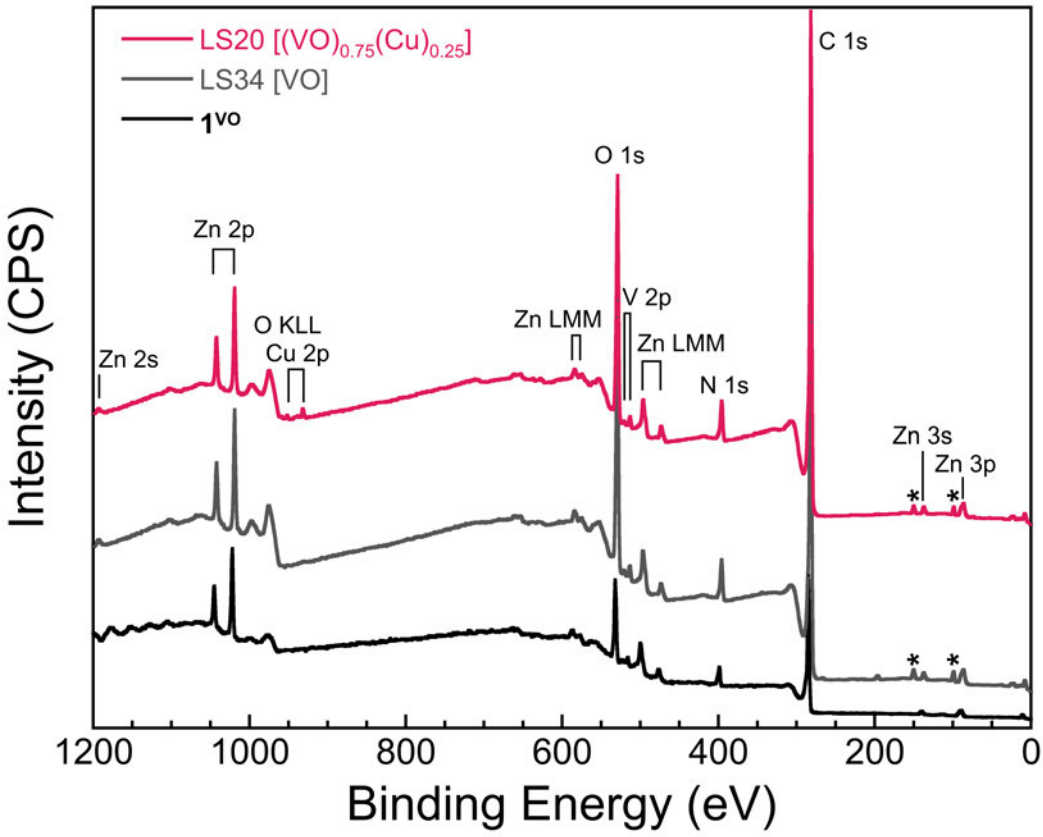

Figure S17. X-ray photoelectron survey spectra of a 34-layers [{VO(TCPP)}Zn_2] deposit on Mylar (grey line) and of bulk **1**^{VO} (black line). The survey spectra of a 20 layers [{M(TCPP)}Zn_2] deposit on Mylar obtained by expanding a 0.75:0.25 mixture of [VO(H_4TCPP]:[Cu(H_4TCPP)] (red line) is also shown, exhibiting the presence of both Cu 2p and V 2p bands.

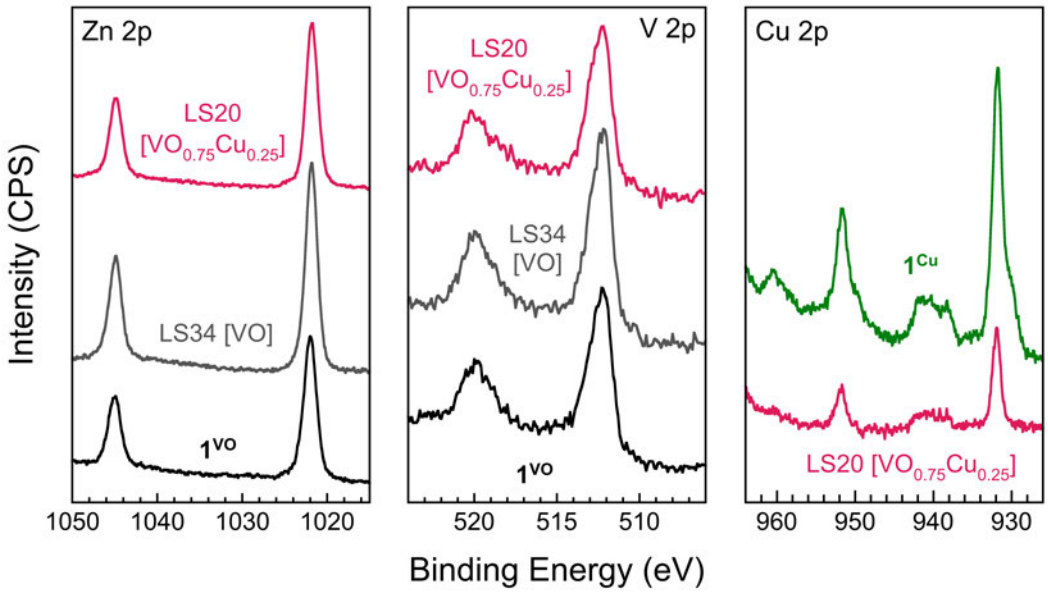

Figure S18. X-ray photoelectron high resolution spectra of the Zn 2p (left) and V 2p (middle) areas of a 34-layers [{VO(TCPP)}Zn_2] deposit on Mylar (grey lines) and of bulk **1**^{VO} (black lines) and a 20 layers [{M(TCPP)}Zn_2] deposit on Mylar obtained by expanding a 0.75:0.25 mixture of [VO(H_4TCPP]:[Cu(H_4TCPP)] (red lines). Full scales are respectively 40000, 3500 and 7000 CPS. The relative V/Zn atomic ratio of the 34-layers [{VO(TCPP)}Zn_2] deposit on Mylar is 0.35. Right: high resolution spectra of the Cu 2p area of the latter mixed metal deposit (red line) and bulk **1**^{Cu} (green line). The relative V/Cu and V+Cu/Zn atomic ratios of the 20-layers [{M(TCPP)}Zn_2] deposit on Mylar are respectively 1.33 and 0.38.

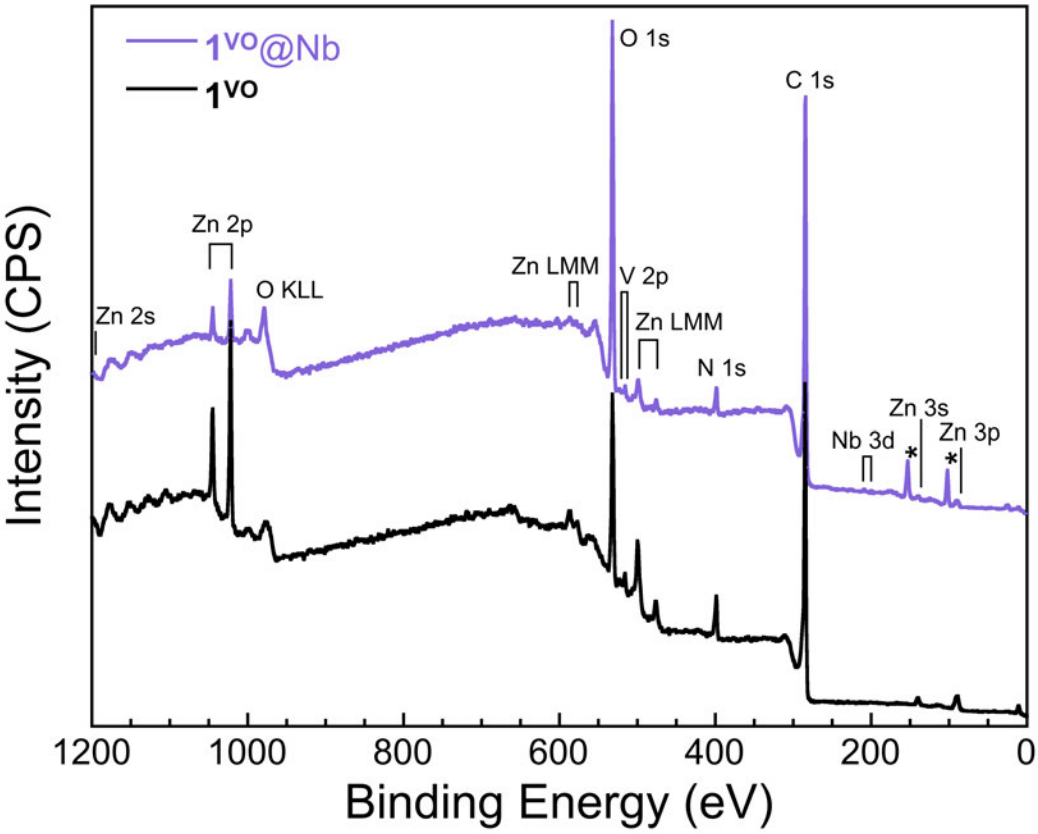

Figure S19A. X-ray photoelectron survey spectra of the [{VO(TCPP)}Zn_2] deposit formed in-situ on the Nb line (purple line) and of bulk **1**^{VO} (black line).

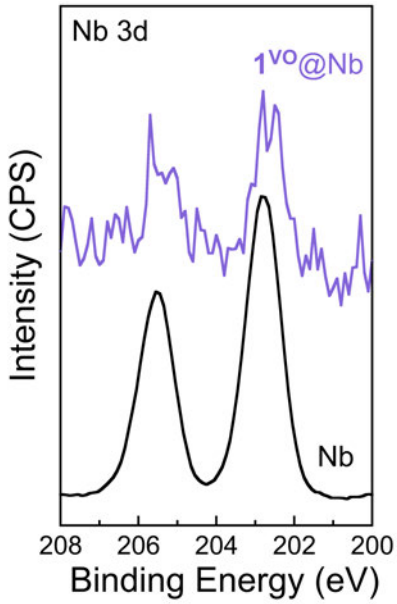

Figure S19B. High resolution spectra of the Nb 3d area for the [{VO(TCPP)}Zn_2] deposit formed *in-situ* (purple line) and for the bare Nb line (black line).

H) UV-Visible Spectroscopy

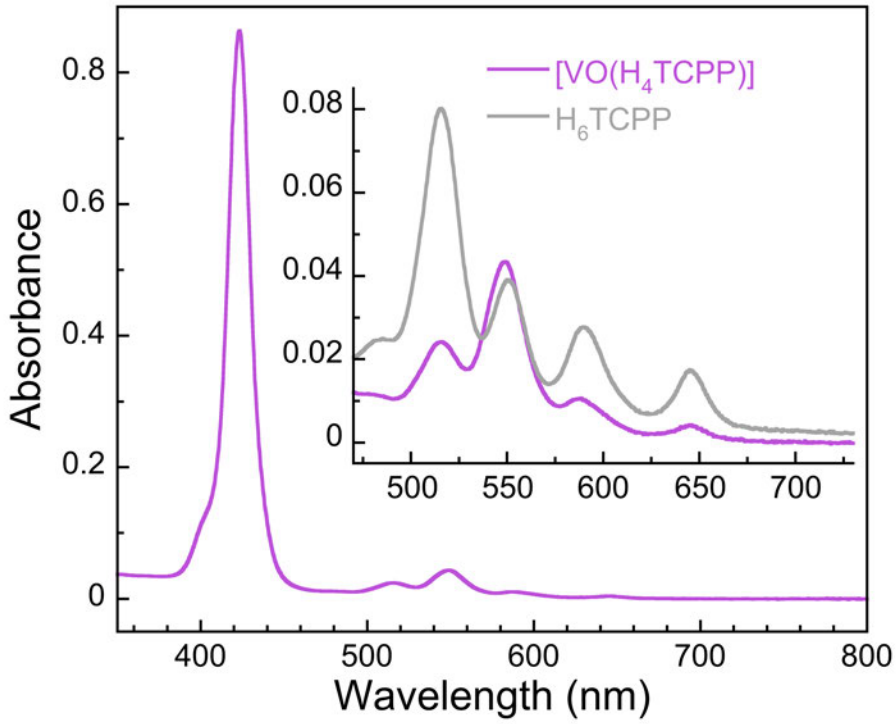

Figure S20. UV-Visible spectrum of a $CHCl_3$:MeOH 3:1 0.03 mM solution of the [VO(H_4TCPP)] precursor (pink line). The inset highlights the Q-band area, comparing with the spectrum of a $CHCl_3$:MeOH 3:1 0.0368 mM of the free-base H_6TCPP (grey line).

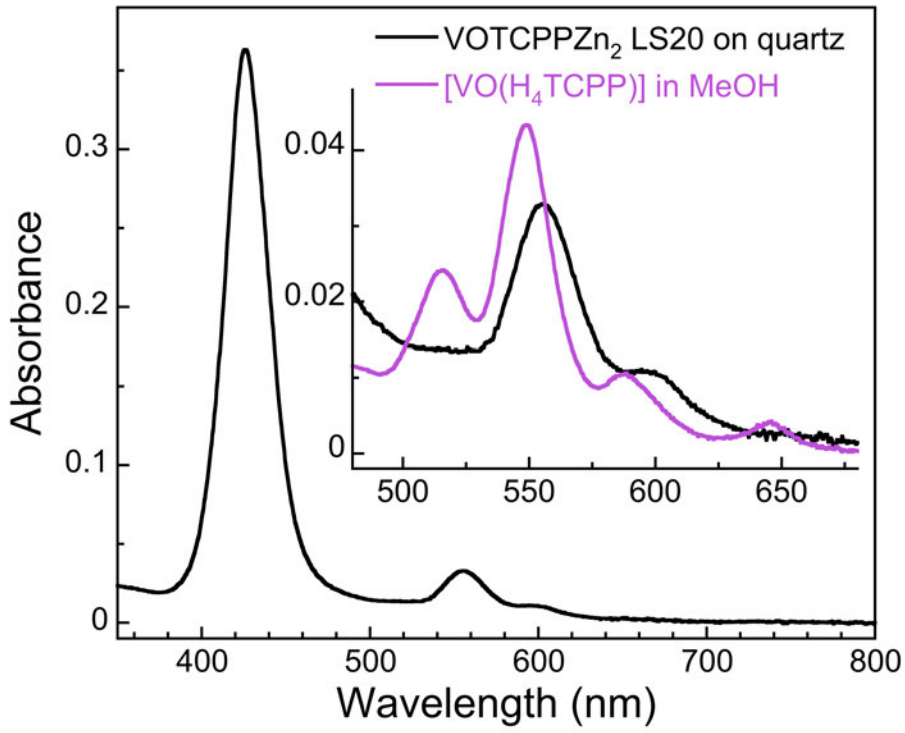

Figure S21. UV-Visible spectrum of a 20-layers [{VO(TCPP)}Zn_2] deposit on quartz (black line). The inset highlights the Q-band area, comparing with the spectrum of a MeOH 0.1 mM solution of the [VO(H_4TCPP)] precursor (pink line).

I) Atomic Force Microscopy

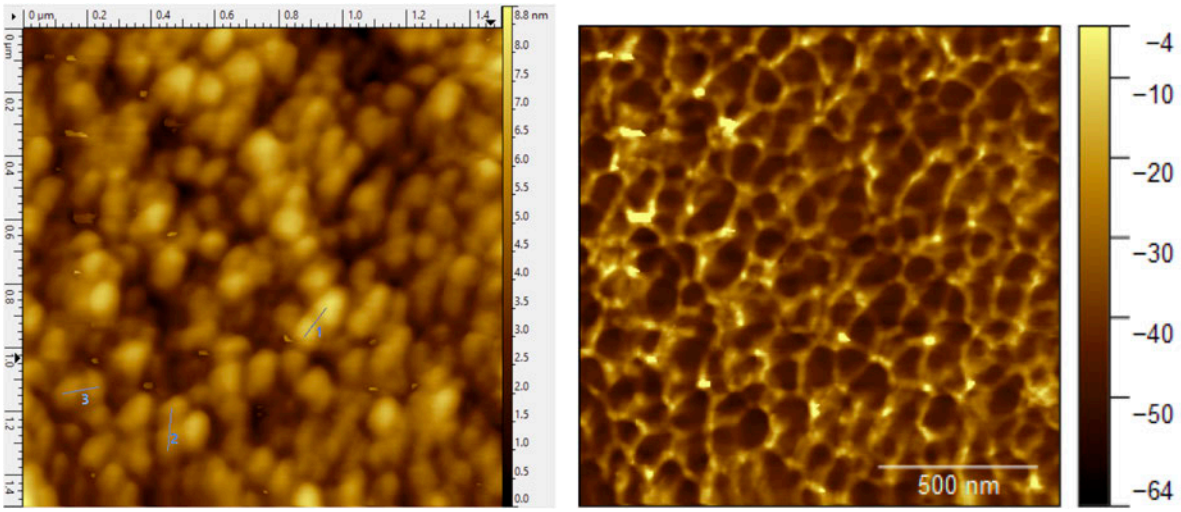

Figure S22. AFM image of the deposit formed on Mylar after 34 transfer cycles of [{VO(TCPP)}Zn_2] nanodomains. Left: topography image shows rounded nanodomains of *ca.* 1 nm height, with an overall rms roughness of 1.26 nm. Right: phase image shows a full and homogeneous surface coverage.

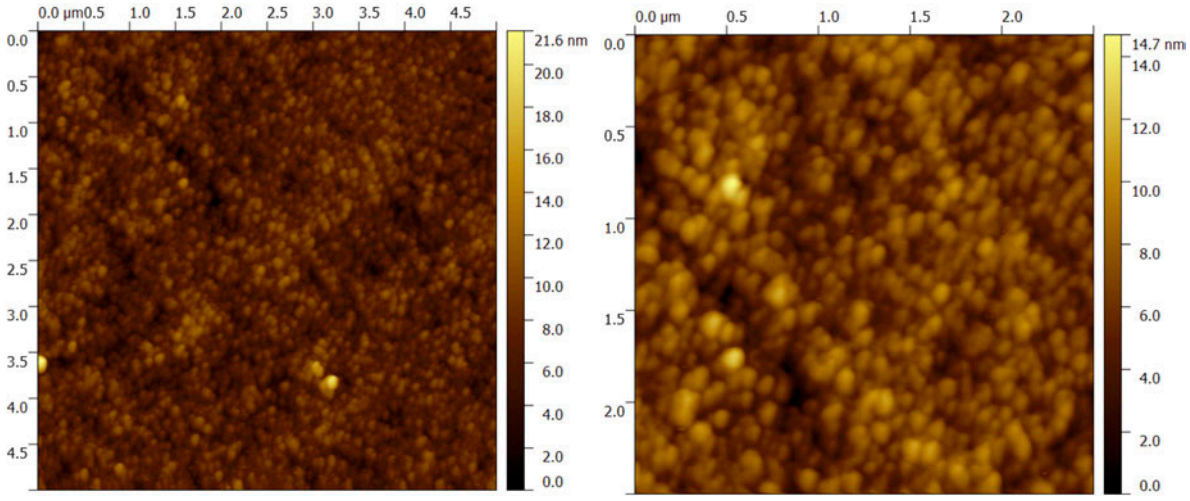

Figure S23. Two larger area AFM topography images of the deposit formed on Mylar after 34 transfer cycles of [{VO(TCPP)}Zn_2] nanodomains.

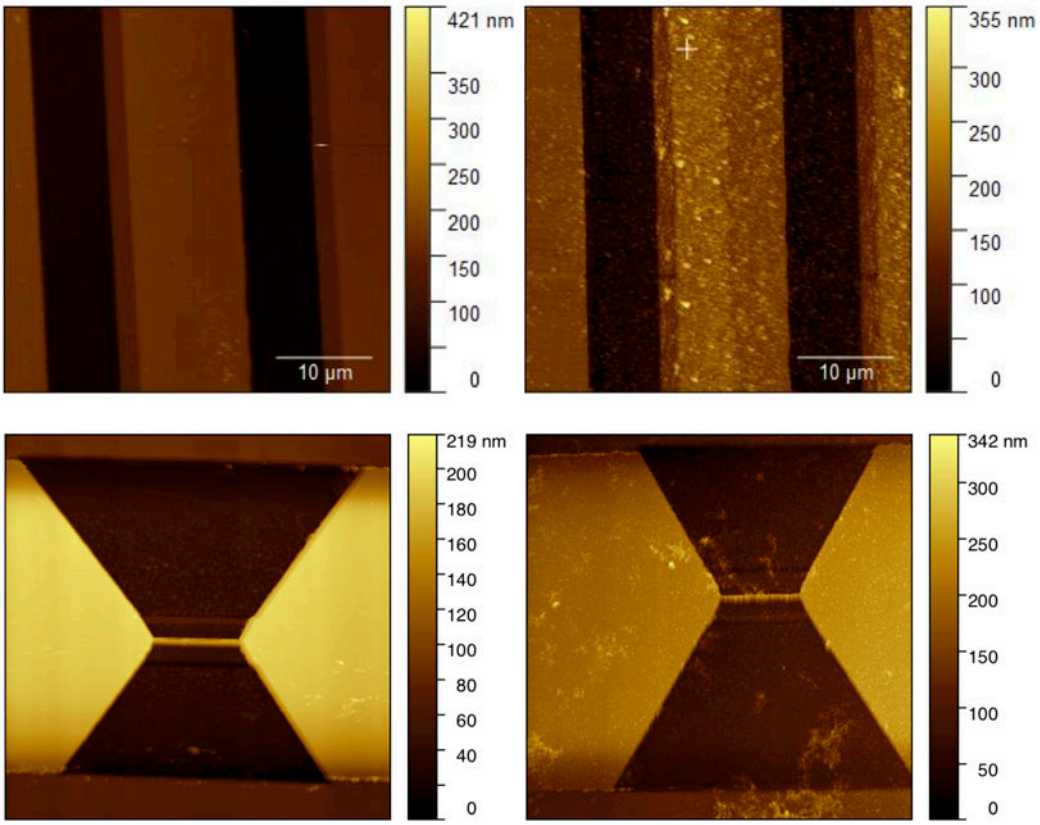

Figure S24. AFM topography images before (left) and after (right) the in-situ formation of nanodomains of the MOF [{VO(TCPP)}Zn_2], on respectively a superconducting resonator with a central 10 μm line (top) and one with a 100 nm wide constriction in the central line (bottom). The top images are 40 x 40 μm^2 while the bottom images are 20 x 20 μm^2.

J) Transmission measurements with on-chip resonators

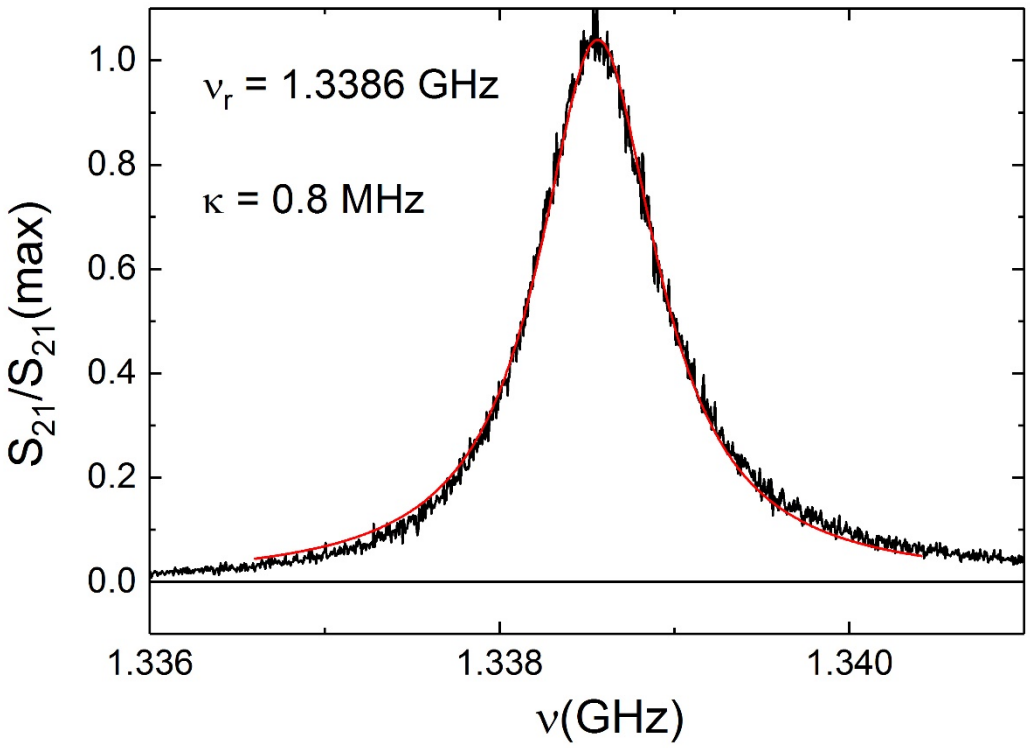

Figure S25. Transmission of the coplanar resonator measured at H = 0. The red solid line is a least square Lorentzian fit, which allows the determination of the resonant frequency of the cavity ν_r and of the photon decoherence time κ.

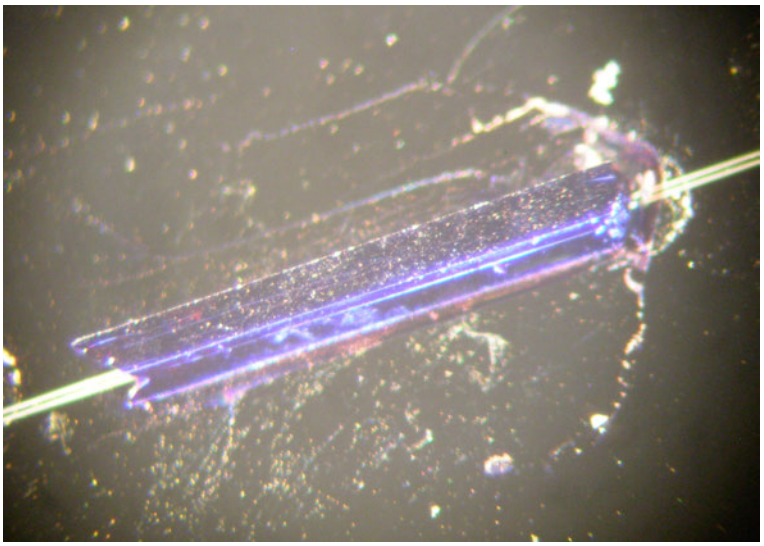

Figure S26. Picture of the single-crystal of [VOTCPPEt] on the resonator superconducting lines.

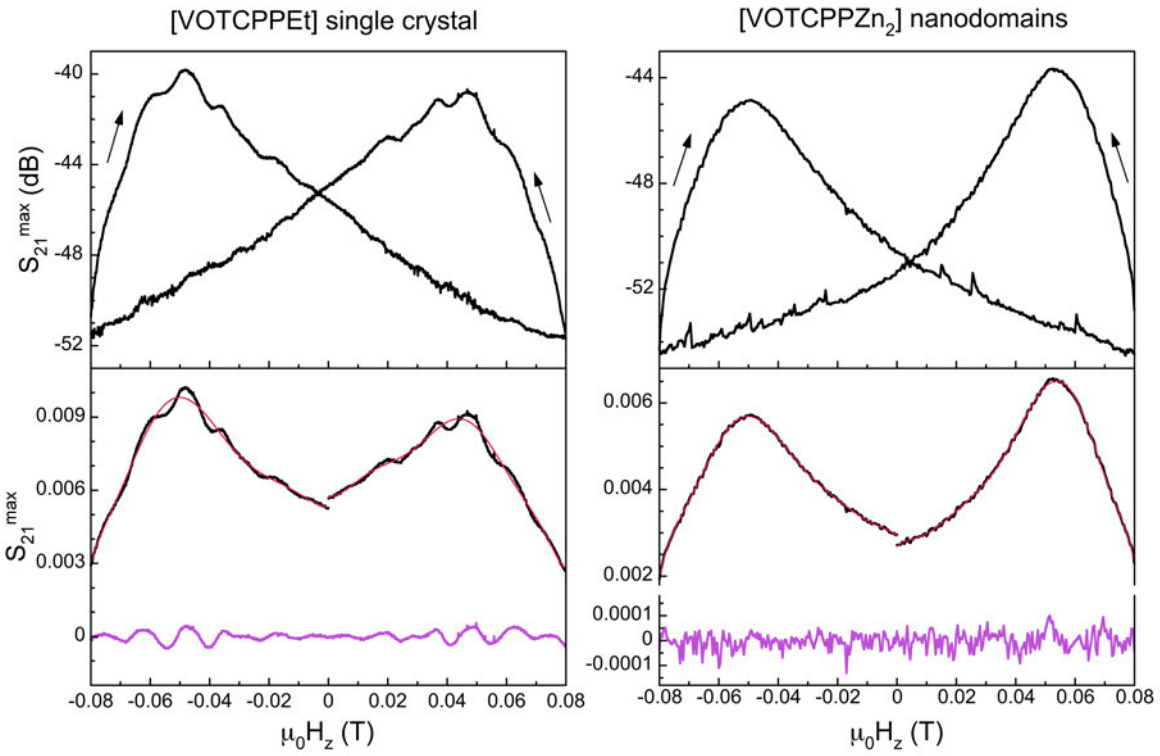

Figure S27. Procedure used to substract the empty resonator response to the experimental maximum peak transmission S_{21}^{max} for a single-crystal of [VO(TCPPEt)] (left) and nanodomains of the MOF [VO(TCPP)Zn_2] formed in-situ (right). Top: raw field dependence of S_{21}^{max} top for both series of measurements, with arrows indicating the field sweep direction. The hysteretic behavior is associated with the fluctuations and pinning of fluxons. Bottom: a 9th degree polynomial background (full red lines) reproducing the overall field dependence is used as the empty resonator response and substracted to the experimental data, yielding the residual curve shown as full purple lines. These are then normalized to give the data shown in Figures 9 and S28. The same procedure has been used for Q and κ.

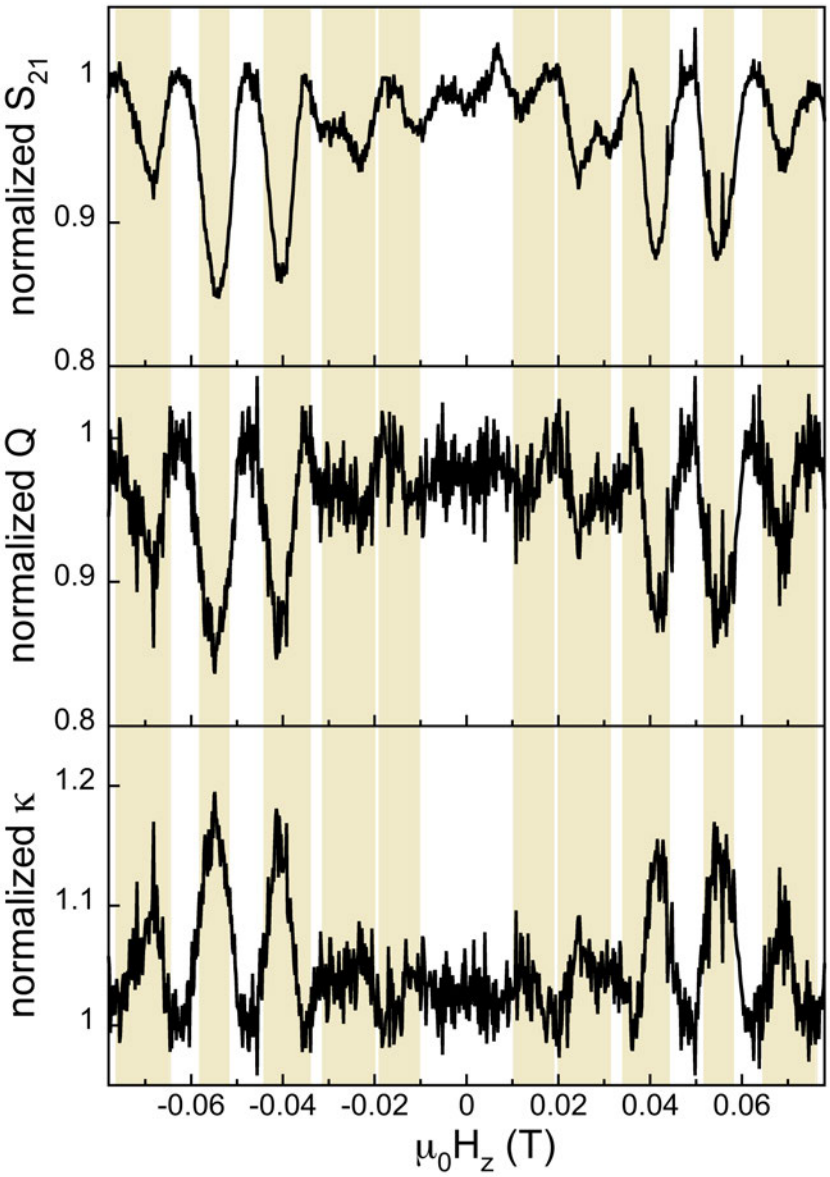

Figure S28. Normalized resonant peak transmission S_{21} (top), quality factor Q (middle) and width κ (bottom) of a 1.34 GHz coplanar resonator coupled to a single-crystal of [VO(TCPPEt)]. The data have been corrected for the empty resonator signals before normalization as shown in Figure S27. Vertical coloured background highlight the field ranges for which the different spin transitions corresponding to the SH used to reproduce the EPR spectra of $\mathbf{1}^{\mathbf{VO}}$ (each for a different nuclear spin state) are expected to become resonant with the cavity photons.

The coupling strength depends on the relative position of the qubit with respect to the local field and on the relative spin state population. It was estimated using the following expression:[2]

$$G_1 = g(\vec{r}_j) = \frac{g_S \mu_B}{\sqrt{2}} \left| \langle G \left| \vec{b}(\vec{r}_j) \vec{S} \right| E \rangle \right| \times \sqrt{\Delta P}$$

where $\vec{b}(\vec{r}_j)$ describes the field generated by the resonator at the position $\vec{r}_j$, *G* and *E* are the ground and excited states of the two-level system defining the qubit, and ΔP describes the difference in thermal population of these states.

We used the numerically calculated field distribution $\vec{b}(\vec{r}_j)$ previously reported.[3]

[2] M. Jenkins, T. Hümmer, M. J. Martínez-Pérez, J. J. García-Ripoll, D. Zueco, F. Luis, *New J. Phys.*, 2013, **15**, 095007
[3] M. D. Jenkins, D. Zueco, O. Roubeau, G. Aromí, J. Majer, F. Luis, *Dalton Trans.*, 2016, **45**, 16682